Diagnosis of Local Gravity Wave Properties during a Sudden Stratospheric Warming

Lena Schoon[1] and Christoph Zülicke[1]

[1]Leibniz-Institute of Atmospheric Physics, Schlossstrasse 6, 18225 Kühlungsborn, Germany

Correspondence to: Lena Schoon (schoon@iap-kborn.de)

Abstract. The selective transmission of gravity waves through an inhomogenous mean flow is investigated. For the local diagnosis of wave properties we develop, validate and apply a novel method which is based on the Hilbert transform and is named "Unified Wave Diagnostics" (UWaDi). Thus, it provides wave properties at any grid point for any wave-containing data. UWaDi is validated for a synthetic test case comprising two different wave packets. In comparison with other methods, the perfomance of UWaDi is very good with respect to wave properties and their location. For a practical application of UWaDi, a minor sudden stratospheric warming on 30 January 2016 is chosen. Specifying the diagnostics on hydrostatic gravity waves in analyses from the European Centre for Medium-Range Weather Forecasts, we confirm locally different transmission through the middle atmosphere. These are interpreted in terms of columnar vertical propagation using the additionally diagnosed local wave numbers. We also note some hint on local gravity wave generation by the stratospheric jet.

1 Introduction

The importance of gravity waves (GWs) for the dynamics of the Earth's atmosphere is without controversy. They influence dynamics from planetary scales to turbulent microscales and play an important role in the middle atmosphere (Fritts and Alexander, 2003). Here, we want to introduce a new method named "Unified Wave Diagnosis" (UWaDi). The method provides phase-independent local wave quantities like amplitude and wave number without any prior assumption. In the following, we want to develop, validate and apply the novel method. The application concentrates on the analysis of GWs for locally varying background wind conditions in the winter 2015/16.

In the past, several methods were developed to estimate wave properties like amplitudes and wave number vectors. A common approach to obtain vertical wave numbers and GW frequency of high-passed filtered wind fluctuations are Stokes parameters (Vincent and Fritts, 1987). This method is based on the definition of polarisation relations and works for single-column measurements. It provides the wave properties in preselected vertical height sections of finite lengths. Next to its original application on radar measurements it is used for radiosonde data (Kramer et al., 2015). A supplement to this method named DIV was introduced by Zülicke and Peters (2006). It determines the dominating harmonic wave in a box from the first zero-crossing of the auto-correlation function. The maximal dectectable wavelength is restricted by the box size. The analysed quantity is the horizontal divergence to get the ageostrophic flow without numerical filtering. A further technique is based on sinusoidal few wave fits (S-3D) (Lehmann et al., 2012). This method was created for the analysis of binned data from remote sensing

(Ern and Preusse, 2012; Ern et al., 2014, 2017; Krisch et al., 2017) but is also applicable to model data (Preusse et al., 2014). The first two modes with highest variance are taken from a fit that minimises the variance-weighted squared deviations over all points in a box. Only a small number of sinusoidal curves are fitted and there might remain uncovered variances in the analysis volume. All these methods have in common, that the analysed spatial scales are dependent on the predefined analysis box size and the assumption of spatial homogeneity of the wave field in these boxes. Nevertheless, these methods are superior to a classic Fourier transform in that point that they allow to search for waves with bigger wavelengths than the box size. Here, we want to develop a method which provides wave parameters locally, meaning at each grid point.

Another three-dimensional spectral analysis method is the 3-D Stockwell-transform (3D-ST) (Wright et al., 2017). This method is capable of analysing the full range of length scales sampled in satellite data and is not restricted to box sizes. At every grid point, a local wave spectrum is estimated. With this method available local wave quantities are wavevectors, amplitudes, phase and group velocities, temporal frequencies and momentum fluxes. However, directions of vector quantities have to be fixed by seperate assumptions. Both, S-3D and 3D-ST look for the largest spectral amplitude to calculate the wave quantity at the respective box point. This might lead to a loss of information, in any case the estimated variance is too small. We search for a method which detects the full variance in each data point.

With UWaDi we find the dominating wave with the Hilbert transform. It makes data binning into boxes redundant and is developed to work with equally-gridded data. In general, the Hilbert transform can be applied to data of any dimensionality. Wave properties such as the amplitude are estimated phase-independently. Every variable including any kind of wave-like structure is analysable and preselection of modes is avoided. Zimin et al. (2003) used the method to obtain the envelope of a train of Rossby waves in one dimension. A supplement was made for waves not in-line with grids by an extension of the formulation to stream lines to obtain quasi-one-dimensional wave packets (Zimin et al., 2006). Kinoshita and Sato (2013) provide a three-dimensional application on Rossby and GWs. Our method comes up with an enhancement for three dimensions and the additionally provision of the wave number in every dimension which was not presented before. We aim to cover the retrieval of local wave properties from arbitrary orientated wave packets. Amplitude and wave number are sampled on the same grid as the input data. After the mathematical description of the method it will be validated with synthetic datasets to demonstrate its quality in comparison with other methods.

For a practical application in geophysical context, we will investigate GWs. Their sources are usually found in the troposphere where waves are generated by flow over orography, convection, frontal systems and jet imbalances. These waves propagate upwards with increasing amplitudes and break in the middle atmosphere where they deposit their momentum to the background flow. Strong influence is exerted on global circulation patterns in the mesosphere as well as in the stratosphere (Holton, 1983; Garcia and Solomon, 1985). GWs play crucial roles in the modulating of the quasi-biennial oscillation (QBO) and the Brewer-Dobson circulation (Dunkerton, 1997; Alexander and Vincent, 2000; Ern et al., 2014). Another stratospheric phenomenon where GWs play a role are sudden stratospheric warmings (SSW). A variety of definitions exists (Butler et al., 2015), but the most common one is given by the World Meteorological Organization stating that a SSW is characterised by a reversal of the $60°$ N to $90°$ N-temperature gradient. Major warmings are associated with a wind reversal at 10 hPa and $60°$ N; minor SSWs (mSSWs) with a wind deceleration at 10 hPa and $60°$ N, where the prevailing westerlies are not turned into easterlies. Even

though planetary waves are the most important drivers of SSWs (Andrews et al., 1987), GWs are affected by the differing background wind conditions during SSWs and are suspected to modulate the polar vortex in the postwarming phase of a SSW (Albers and Birner, 2014). The coupling of GWs with planetary waves during a SSW was investigated by simulations and different measurement techniques. Restricted to zonal mean wave properties, local eastward propagating GWs can only be estimated by anomalies in horizontal divergence fields. Nonetheless, these GWs are, next to selective transmission, assigned to GW emission and unbalanced flow adjustment (Yamashita et al., 2010; Limpasuvan et al., 2011). We are interested in the longitude-dependent transmission of GWs during a SSW. Pioneering work was done by Dunkerton and Butchart (1984). They analysed model data and found that selective transmission of GWs during a SSW is dependent on longitude. Therefore, regions where vertical wave propagation is inhibited exist as well as regions where waves can propagate up to the mesosphere. The analysis of Dunkerton and Butchart (1984) was restricted to parameterized GWs of the "intermediate range", that they defined between 50 km and 200 km. They state that it remains unclear, in what kind GWs of larger scale will act during SSWs. A study on a self-generated SSW in a model showed that GWs reverse the circulation in the mesosphere-lower thermosphere during a SSW by altering the altitude of GW breaking. This altitude is highly dependent on the specification of GW momentum flux in the lower atmosphere (Liu and Roble, 2002). This is where our analysis sets in. We want to diagnose the appearance of GWs precisely in space and give an interpretation using the information on their changing amplitude and wave number. For that purpose, we will use UWaDi with a GW-specific diagnostic.

The northern winter 2015/16 brought up several interesting features, including several issues of GW behaviour. The beginning of the winter was characterised by an extraordinarily strong and cold polar vortex driven by a deceleration of planetary waves in November/December 2015 (Matthias et al., 2016). Thereinafter, for the end of that winter a record Arctic ozone loss was expected (Manney and Lawrence, 2016). Furthermore, the extraordinarily polar vortex caused a southward shift of planetary waves leading to anomalies in the QBO (Coy et al., 2017). Inbetween, a joint field campaign of the research projects MET-ROSI, GW-LCYCLE 2 and PACOG took place in Scandinavia in January 2016. Stober et al. (2017) found a summer-like zonal wind reversal in the upper mesosphere lasting until the end of January 2016, leading to different GW filtering processes in the mesosphere compared to usual winter-like wind conditions. During the field campaign first tomographic observations of GWs by an infrared limb imager provide a full three-dimensional picture of a GW packet above Iceland (Krisch et al., 2017). Additionally, a remarkable comparative study shows that forecasts of the current operational cycle (41r2) of the European Centre for Medium-Range Weather Forecasts (ECMWF) Integrated Forecast System (IFS) shows good accordance with space-borne lidar measurements while picturing large-scale and mesoscale wave structures in polar stratospheric clouds (Dörnbrack et al., 2017). We choose the mid-winter of 2016 for an application of UWaDi because it is very well sampled with observations of GW properties. Hopefully, we may provide additional impulses to the evaluation of observations.

In particular, UWaDi requires regular gridded data. Assimilated data products from ECMWF are suitable to analyse local phenomena and their coupling as they resolve essential parts of GW dynamics in the stratosphere. Even the T799 resolution gives proof of correct GW appearance in the stratosphere. Validation with satellite measurements point out that ECMWF captures GWs well in the mid- and high-latitudes (Yamashita et al., 2010; Preusse et al., 2014). The improved T1279 resolution yields to a bigger portion of resolved GWs in ECMWF data. Validation studies with measurements show that mid-latitude GWs

are captured well being driven by orographic and jet-stream associated sources (Shutts and Vosper, 2011; Jewtoukoff et al., 2015). Our approach concentrates on fields of horizontal divergence of ECMWF IFS data. The horizontal divergence counts for a dynamical indicator for GWs (Plougonven et al., 2003; Zülicke and Peters, 2006). Its magnitude was found to correlate with temperature anomalies induced by mountain waves (Dörnbrack et al., 2012; Khaykin et al., 2015). We concentrate on vertical propagation only, highlighting selective transmission. Studies arguing the restrictions on vertical-only propagation can be found in Yamashita et al. (2013), Kalisch et al. (2014) and Ehard et al. (2017). We point out that meridional propagation of GWs can play an important role for the analysis of the deposition of GW drag in the mesosphere. As we give an idea of GW propagation in the upper troposphere and stratosphere we concentrate on vertical propagation and are aware of the possibility of GW entrainment of strong winds.

The paper is organised as follows. After providing a step-by-step introduction and validation of the novel method in Section 2, we give a short overview of the estimation of wave quantities for synthetic data and describe the analysis data. In Section 3 we show our results for the mSSW on 30 January 2016 where we study local GW generation and propagation. The discussion of our results in Section 4 is followed by the Summary and Conclusion (Sec. 5).

2 Method and Data

In this section we develop and validate an algorithm to extract wave parameters from three-dimensional data. For local diagnosis of waves, phase-independent estimates of wave amplitudes as well as the wave vector are essential. For this, we employ the Hilbert transform (Von Storch and Zwiers, 2001). The Hilbert transform shifts any sinusoidal wave structure by a quarter phase, i.e. turning a sine into a cosine. By constructing a new complex number consisting of the original field as real part and its Hilbert transform as the imaginary part, the absolute value is always the amplitude (square root of squared real and imaginary part). The amplitude is independent of the phase and the wavelength of the oscillation and there is no need of any explicit fitting of a wave. In addition, the absolute wave number in all three dimensions is determined from the phase gradient.

2.1 Step-by-step outline of the method

In the following we introduce UWaDi by a step-by-step outline. Further, we validate it with a well-defined test wave packet in comparison with other methods. In general, UWaDi is a script package which allows the user to steer data preprocessing, the main wave analysis and data plotting, from a set of namelists. This package is coded in open source software such as NCL and Fortran. Its multi-purpose applicability on a set of arbitrary waves, e.g. gravity waves or planetary waves, defines its unified character.

1. Firstly, the three-dimensional gridded data is preprocessed. UWaDi requires data from equidistant grids. Horizontally, the grids are equidistant if they are provided on a regular latitude-longitude grid. The latitude-dependence of grid distance

is taken into account. Vertical interpolation from model levels to equidistant height levels is performed by associating constant heights with pressure levels. This might cause problems in areas of high orography and inside the planetary boundary layer. Both are avoided in the following application. Consider to first separate the fluctuations from the background with appropiate numerical or dynamical filters.

2. The underlying Hilbert transform starts with a Discrete Fourier Transform (DFT) which creates a complex series in wave number space f_k from the real valued data f_x (e.g. Smith et al. (1997)):

$$f_k = \text{DFT}(f_x) \tag{1}$$

3. DFTs can be biased by variance leakage through side lobes in spectral space. Tapering methods abandon this but can smear out nearby wave numbers. A loss of absolute amplitude can be overcome by using normalised weights (Von Storch and Zwiers, 2001). For the present study, however, the best results were obtained by turning the taper off.

4. In wave number space a rectangular bandpass filter reduces the complex series to the user-predefined wave number limits k_{min} and k_{max}. Here, we make sure that only waves of the considered range of wave numbers are used for the following analysis.

$$f_{k,filtered} = F(k_{min}, k_{max}) f_k, \tag{2}$$

5. To get back from wave number space an inverse DFT is performed.

$$\hat{f}_x = 2 * \text{DFT}^{-1}(f_{k,filtered}). \tag{3}$$

6. The such constructed complex valued function $\hat{f}_x$ of the input data f_x as the real part and the Hilbert-transformed function $H(f_x)$ as the imaginary part

$$\hat{f}_x = f_x + iH(f_x) \tag{4}$$

provides the amplitude a_x (Schönwiese, 2013)

$$a_x = |\hat{f}_x| = \sqrt{f_x{}^2 + H(f_x)^2} \tag{5}$$

and the phase estimate Φ_x

$$\Phi_x = \text{atan}\left(\frac{H(f_x)}{f_x}\right). \tag{6}$$

7. The phase gradient is a measure of wave number

$$k_x = \frac{d\Phi_x}{dx} \approx \frac{\left|\text{DFT}^{-1}(k\text{DFT}\hat{f}_x)\right|}{|\hat{f}_x|}. \tag{7}$$

8. Due to the finite character of the data series it may happen that high-frequency fluctuations appear after the Hilbert transform. We neglect those by applying a low-pass filter. We smooth over a number of grid points determined by the lower wave number limit k_{min}.

9. Alienation of outliers is taken care of by two different quality. Firstly, the amplitude and wave number are checked for at least a half undamped wave. Therefore, the packet length l_x is essential. It is calculated by covariance functions C_{xx}:

$$l_x = \sum_{x=0}^{x_{max}} \left| \frac{C_{xx}}{C_{00}} \right| \tag{8}$$

with $x_{max} = \frac{N-1}{5}$ (Chatfield, 2016). This method goes back to Zülicke and Peters (2006). The quality check then is defined by the inequality

$$k_x l_x > \pi. \tag{9}$$

Secondly, the retrieved signals are supposed to lie above the noise level of the input data. An empirical threshold c checks the amplitude for being valid considering the standard deviation of the input horizontal divergence δ

$$a_x > c * \delta(f_x). \tag{10}$$

Empirically, we use $c = 0.01$. This idea follows Glatt and Wirth (2014).

UWaDi uses a quality flag $q = 1$ which is set to false ($q = 0$) if at least one quality check is rejected.

10. Steps 2 to 7 are repeated for the other dimensions (y, z).

11. Amplitude and absolute wave number are saved on the same grid as the input data to create a full three-dimensional analysis of local wave quantities. The amplitude is combined to a wave number-weighted sum of the three spatial dimensions

$$a_{(x,y,z)} = \left(\frac{\sum_{d=x,y,z} q_d k_d^2 a_d^2}{\sum_{d=x,y,z} q_d k_d^2} \right)^{\frac{1}{2}}. \tag{11}$$

The absolute wave number is determined by

$$k_{(x,y,z)} = \left(\sum_{d=x,y,z} q_d * k_d^2 \right)^{\frac{1}{2}}, \tag{12}$$

with d denoting the spatial index.

The method provides an exact measure of the amplitude in the sense of the sum of squared amplitudes of the wave modes. The dominating wave number is the amplitude weighted sum of all. Spectrally wide dynamics can cause a significant reduction of information (Appendix A). Applying UWaDi with several narrow band-pass limits would provide information on spectrally spread waves. However, the method is recommended for the first guess of the dominant wave packet.
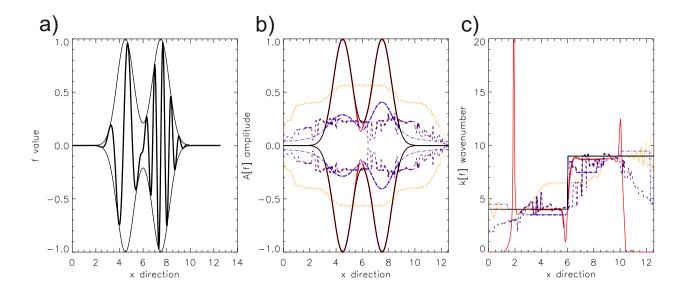
Figure 1. One-dimensional test function (bold line, left figure) adapted from Zimin et al. (2003) and its envelope. Comparison of amplitude (centre) and wave number (right) calculated by different methods: UWaDi (solid, red), DIV (dotted, orange), S-3D (dashed, violet) and 3D-ST (dash-dotted, blue). Valid estimates are drawn in bold.

2.2 Validation of the method

For a comparison of available methods that obtain wave quantities we choose the test case presented in Zimin et al. (2003) (Fig. 1a). A couple of localized wave packets with the wave numbers 4 and 9 is given in one dimension on the interval $[0, 4\pi]$ by

$$f_x = \exp\left(-(x-4.5)^2\right)\cos(4x) + \exp\left(-(x-7.5)^2\right)\cos(9x). \tag{13}$$

Here, the quality check (step 9) requires the amplitudes to exceed half of the sample standard deviation.

The method showing the best agreement with the theoretical value is UWaDi (Fig. 1b). For the amplitude both wave packets are clearly distinguishable and the maximum peaks are recovered exactly. As expected, the 3D-ST method shows a rebuilding of the wave packet's shape as well. The lack of absolute amplitude value might be overcome with empirical correction factors Nevertheless, the amplitudes of both wave packets differ from each other. A higher peak of amplitude is given by the DIV method but the two wave packets are smeared out. A similar pattern is shown for the S-3D method. Both latter methods show high dependence on the chosen box size withing the analysis. The wave number calculation is best for UWaDi (Fig. 1c). The high peaks at the beginning and end of the wave packets are sorted out by the quality check. S-3D and 3D-ST show good

7

results in peaking at the right value but do not cover the complete spatial range of the wave packet. Wave number calculation of DIV shows higher deviations. Altogether, UWaDi shows nearly perfect agreement with the theoretical expectations.

2.3 Analysis data

ECMWF data from the IFS operational cycle 41r1 is chosen for this analysis. Together with the latest cycle 41r2 it is based on T1279 L137 but differs in its effective horizontal resolution and non-orographic gravity wave parameterization. Cy41r2 reduces the distance between grid points to 9 km, from former 16 km. Not shown comparison studies between IFS data provided on different grid sizes $(0.1°, 0.36°, 1°)$ considering our bandpass filter conditions gave reliable and comparable results for the $0.1°$- and $0.36°$-grids. Therefore, we decide that the former cycle stored with a resolution of $0.36°$ (ca. 40 km) meets our requirements. We discuss resolved gravity waves of a horizontal scale between 100 km and 1500 km. In vertical direction we are interested in gravity waves within the wave length limits of 1 km to 15 km. These scales fullfill the assumption of hydrostatics and cover the range of mid- and low-frequency GWs (Guest et al., 2000).

Vertical propagating GWs are damped in ECMWF IFS products from 10 hPa ($\approx$30 km) upwards (ECMWF, 2016). At 10 hPa the stratospheric sponge starts and a damping of wave propagation is expected (Jablonowski and Williamson, 2011). The mesospheric sponge follows at 1 hPa acting on the divergence and therefore directly on the GW properties. We restrict our analysis to a maxmimum altitude of 45 km and therefore follow the advice of Yamashita et al. (2010). The regular latitude-longitude grid is remained during the analysis. We interpolate model levels to equidistant height levels between 2 km to 45 km with a distance of 500 m.

2.4 Gravity-wave specific quantities

From the diagnosed fields of amplitude and wave number we calculate the kinematic wave energy e and wave action A. In order to find the ageostrophic GW motion we analyse fields of horizontal divergence. The kinematic wave energy is derived from polarisation equations for GWs assuming hydrostatics (Zülicke and Peters, 2006) (Appendix B):

$$e = \frac{\delta^2}{k_h^2}. \tag{14}$$

In this formula we need information on the variance and the horizontal wave number. Both are provided by UWaDi.

$$\delta^2 = \frac{a^2}{2} \tag{15}$$

$$k_h^2 = k_x^2 + k_y^2 \tag{16}$$

The wave action is a conserved quantity describing waves in presence of an imhogeneous background wind field (Bretherton, 1966). It does not change for upward propagating wave as long as they do not interact with the mean flow. wave action is

defined by putting the kinematic wave energy e in relation to the intrinsic (flow-relative) frequency ω:

$$A = \rho \frac{e}{\omega}, \tag{17}$$

ρ being the density. The intrinsic frequency ω is calculated with the dispersion relation in mid- and low-frequency approximation: $\omega^2 = f^2 + \frac{N^2 \left(k_x^2 + k_y^2 \right)}{k_z^2}$.

5   From $A = \rho \frac{e}{\omega} =$ constant, one can see the following

- density effect: $e \propto \frac{1}{\rho} \propto \exp\left(\frac{z}{H}\right)$. The above derived energy undergoes an exponential increase according to the density with the scale height H in vertical direction z.

- wind effect: $e \propto \Omega$. From the apparent (ground-based) phase speed $c = \frac{\omega}{k} + u$ one gets the dependence of the intrinsic frequency: $\omega = k(c - u)$. Assuming constant phase speed c and a constant wave number k for a wave packet, meaning
10   that a wave is propagating in a horizontally homogenous wind $u(z)$, the energy scales with the background wind u.

For the following analysis primarily wave action is used.

3   Results

A minor SSW occured on 30 January 2016. Fig. 2a shows the wind velocity of the northern hemisphere at 10 hPa. A vortex displacement from the pole is visible. The jet streak above northern Europe is decelerating. The displaced vortex causes areas
15   of strongly curved winds. The horizontal divergence as a measure of GWs shows high wave activity above northern Europe aligned cross-stream. Equal patterns appear above eastern Siberia, corresponding to another area of a decelerating and bent wind streak. UWaDi applied on the field of horizontal divergence provides GW amplitude and wave action (Fig. 2c, d). Areas of high orography like the Tibetan Plateau and Greenland are excluded. GW amplitudes show patterns aligned with the horizontal divergence. The wave action shows the highest peak above northern Europe and lower values above eastern Siberia.
20   In the zonal mean the horizontal wave number remains nearly constant with increasing altitude (Fig. 3). In more convenient terms of wavelengths, we find a horizontal variation between 130 km to 165 km. The vertical wave number decreases from the bottom limit to an altitude of 3 km. At the altitude of 10 km where the tropospheric jet is expected it shows a change in gradient. The increase in vertical wave number after 35 km altitude is a feature that occurs in the zonal mean data frequently, independent from the overall synoptic situation and is therefore expected to be an artefact of artifical wave damping from the
25   IFS sponge layer. In wavelength, the vertical wave number in zonal mean varies between 2 km and 5 km.
    We next inspect local profiles in different background wind conditions. Longitude-height sections of zonal wind (Fig. 4a) and wave action (Fig. 4b) at $60°$ N on 30 January 2016 help to find the location of interesting vertical profiles. Three profiles are chosen that are representative for regions of similar filter conditions. We did not find significant differences between spatial averaging over areas of some longitudes extension and the local profiles (not shown). The low-pass filter applied in Step 8
30   helps to overcome massive grid-point to grid-point fluctuations. The first profile ① at $7.56°$ E is chosen to be in a height range characterised by strong zonal eastward winds and lies in the deceleration area of the jet stream above northern Europe. Profile
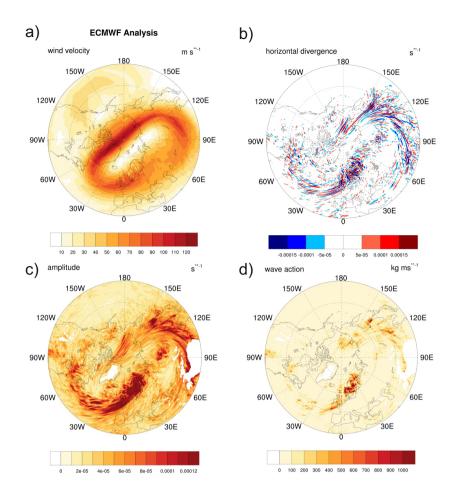
Figure 2. Synoptical situation of the northern hemisphere from ECMWF analysis at 10 hPa on 30 January, 2016. Wind velocity (a), horizontal divergence (b). Gravity wave amplitude (c) and wave action (d).

② is at 151.92° E, therewith in the area of a descented stratospheric jet streak caused by the displacement of the polar vortex. In Fig. 4a it is visible as a wind intrusion in the altitude range between 14 km and 34 km. The wave action shows a peak in that height area (Fig. 4b). For comparison we take a third profile ③ at 240.12° E in a region of low wind velocity, that is: weak tropospheric and weak stratospheric jets.

5   To highlight the advantage of a local wave analysis we plot the zonal mean wave quantities at 60° N on 30 January 2016 (Fig. 5a). One can see the energy scaling with the decreasing density with increasing altitude. Small deviations from the exponential density structure correlate with small jumps in the wave action profile. Overall, zonal mean zonal wind is low with a small maximum hinting at the stratospheric jet stream. Wave action and kinematic wave energy are highly variable below 6 km altitude because of orographic influence. The not trustworthy areas are excluded. Overall, wave action decreases from 10 $1000 \, \mathrm{kg \, m^{-1} \, s^{-1}}$ in the upper troposphere to $100 \, \mathrm{kg \, m^{-1} \, s^{-1}}$ in the middle atmosphere. Further upwards it remains constant.
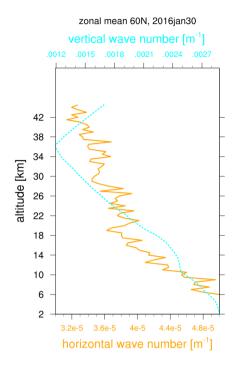
Figure 3. Horizontal (solid, orange) and vertical (dotted, light blue) wave number in zonal mean at 60°N, on 30 January 2016.
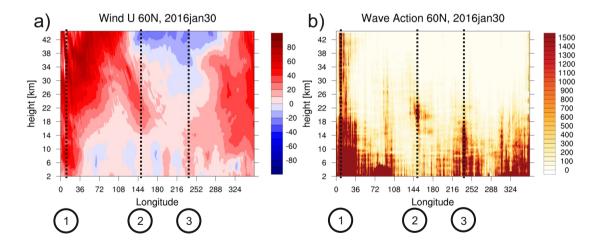

Figure 4. Zonal wind (a) and wave action (b) at 60°N, 30 January 2016 in longitude-height section. Numbered vertical profiles for further analysis are highlighted.

A constant profile of wave action means a constant propagation of GWs without deposition of momentum and therefore no interaction with the mean flow. The wind profile shows low wind speeds. We are interested in selective wave transmission which can not be seen from zonal mean averages. Thus, we provide local profiles.

During a local increase of wind velocity above northern Europe the vertical profiles of ① show that the zonal wind meanders around 50 m s^{-1} (Fig. 5b). The vertical wave number is nearly constant with an average wave length of 8 km and a small minimum after the tropospheric jet with 7 km. The low-pass filter acts on a spatial running average of $k_{min} = 15$km, therefore the wave number does not scale with the wind fluctuations. The wave action shows a high gradient changing from former 10000 kg m^{-1} s^{-1} to 1000 kg m^{-1} s^{-1}, right where the vertical wave number has its maximum at an altitude of 16 km.

Above eastern Siberia a descended stratospheric jet streak appears, jointly with high wave action (Fig. 4). The zonal wind vertical profile ② shows this in a height range of 14 km to 30 km with in increase from 5 m s^{-1} to maximal 30 m s^{-1} (Fig. 5c). The wave action follows the structure of the zonal wind. The vertical wave number shows lower gradients in that altitude range. Altogether, GW emissions seems to take place in the lower stratosphere, clearly above the tropospheric jet stream. GWs of vertical wave length of 2 km can be found.

The last set of vertical profiles is located in an area of low zonal winds ③ (Fig. 5d). In the troposphere eastward winds and in the middle stratosphere westward winds occure. In the altitude of the wind reversal a change of gradient in wave action might show a filter process of GWs. This profile lies in the lee of the Rocky Mountains, hence, mountain waves are most likely.

4 Discussion

The topic of selective wave transmission was first risen up by Dunkerton and Butchart (1984). They highlighted the longitude-dependent gravity wave propagation during a SSW by focussing on the impact on the mesosphere. Ern et al. (2016) further point out that the selective filtering by the anomolous winds during a SSW create heavy impact on GW propagation through the whole atmosphere. They point out theoretically, that during the upwards propagation of GWs, these waves get attenuated or eliminated by distinct specifications of background flows. These findings were obtained with the box-based S-3D algorithm. We add some spatially more refined analysis with UWaDi.

The high-wind case ① showing the highest values of wave action and nearly no changes in the vertical wave number above northern Europe are defined by the longest vertical wave length with 7 km. This long vertical wave length describing steep waves may hint on an orographic excited GW caused by the eastward flow above the scandinavian mountain ridge Kjølen. The location as well as the filtered out short vertical wave lengths suggest this idea and agree with findings of Limpasuvan et al. (2011). The overall high wave action underlines the orographic induced GW packet assumption. This is close to the findings of Krisch et al. (2017), who analysed a wave packet on 25 January 2016 above Iceland, just a few days before our analysis. Mentionable is that from the 25 January to 30 January the overall approaching flow direction did not change above northern Europe and comparable GW characteristics can be expected. Further detailed analysis on this GW packet are expected by upcoming publications according to the joint measurement campaign of METROSI, GW-LCYCLE 2 and PACOG at, amongst others, Kiruna, Sweden (67° N, 20° E).
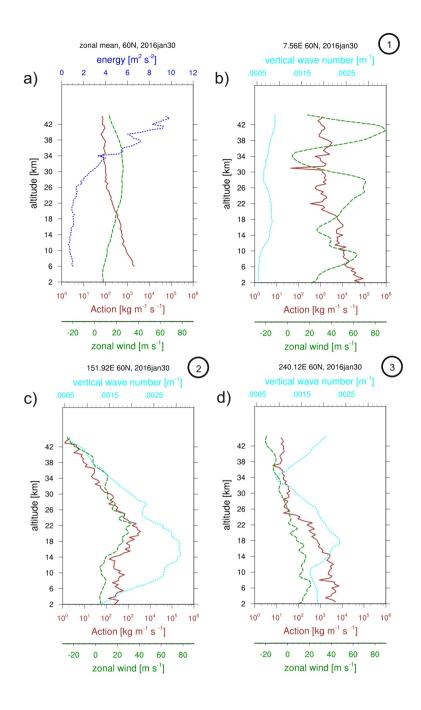
Figure 5. Vertical profiles at 60°N, 30 January 2016. Zonal mean (a) of kinematic wave energy (dotted, blue), wave action (solid, red) and zonal wind (dashed, green). Local vertical profiles at 7.56°E (b), 151.92°E (c) and 240.12°E (d) with the vertical wave number (dotted, light blue), wave action (solid, red) and zonal wind (dashed, green). Local profiles according to markers of Fig. 4.

In the descended stratospheric jet case ② (Fig. 5c) we find a GW packet triggered off a bent and decelerating stratospheric jet. Firstly explained by Uccellini and Koch (1987), jet-exit regions in the troposphere are expected to emit GWs. The increase of wave action in the middle stratosphere according to the intrusion of westerlies seen in Fig. 4a and b leads to the assumption that the present feature is caused by the stratospheric jet. The horizontal divergence field supports this hypothethis with cross-stream aligned fluctuations above eastern Sibera, comparable to the findings in the troposphere by Mirzaei et al. (2014). Further agreements are the higher wave action as well as the lowest shown wavelength in this case of 1.9 km. Wave packets found in jet-exit region are characterised as shallow near-inertial wave packets.

Furthermore, we want to discuss the phenomenon of vanishing GWs at critical wind levels. Stating that waves orthogonal to the mean flow are eliminated due to critical layer absorption occures if the wave vector rotates (Dunkerton and Butchart, 1984). With local vertical profiles of the vertical wave number we find these features above the descended stratospheric jet in ②. The critical level is the level at which background wind and GW phase speed are of same value. There, GWs dissipate and drag is put on the mean flow at lower altitudes than during undisturbed conditions (Wang and Alexander, 2009). Here, a peak in vertical wave number is an indicator for wave absorption according to the mid-frequencies dispersion relation and definition of the Doppler frequency: $k_z = \frac{N}{(c-u)}$. At winds of the order of the phase speed the denominator reduces to zero and the vertical wave number peaks. In an altitude of 28 km we see a peak in the vertical wave number where the zonal wind reaches $u \approx 15\,\mathrm{m\,s^{-1}}$. We find a horizontal phase speed of $c \approx 15\,\mathrm{m\,s^{-1}}$, which measures up with the expectations because jet-generated GWs tend to be fast. The decrease of wave action quantifies the filtering of GWs in this height range. A sharp jump to less wave action is not expected as we apply the low-pass filter and it may take the length of one wave to be filtered out. Furthermore, due to the relative high phase speed no sharp variation at the height of the wind reversal is visible. The near-inertial GWs are not subject of absorption.

In the low-wind case ③ we see that the vertical wave number does not directly scale with the low zonal wind. The high wave action in the upper troposphere up to the height of the wind reversal of 23 km may be caused by orographic induced GWs due to the position in the lee of the Rocky Mountains. Assuming to have orographic quasi-stationary GWs, we get a horizontal phase speed of $c \approx 0\,\mathrm{m\,s^{-1}}$ and do not find absorption at critical levels except at the height of the wind reversal, where a high gradient in wave action is visible. Above that, the overall lowest values of wave action are found, aggreeing with measurements in that height range (Thurairajah et al., 2010). The feature of increasing vertical wave number above an altitude of 35 km fits to our findings before, where in zonal mean vertical wave number we saw the sponge layer of the model to begin to act on GWs (Fig. 3). We suggest, the fact that we do not see this in the other profiles arises from the low wind speeds jointly with low phase speed for this case. In zonal mean we do find low zonal winds as well (Fig. 5a).

5 Summary and Conclusion

With UWaDi we provide a tool for the analysis of any wave-containting data to estimate amplitude and wave number phase-independent and locally. The method is based on a Hilbert transform and returns such an estimate for each data grid point, thus, avoiding the use of pre-defined boxes for a spectral estimate. With regard to the locality it clearly shows its advantages

in a method comparison for an synthetic test case. Disadvantages may play a role when the wave spectrum is broad and the nomination of one dominant harmonic is not justified. The additional estimation of the wave numbers completes the elements of a wave packet description. Their sign is not fixed which is the case for all spatial analysis methods. However, the method is recommended as a reliable local estimate of medium complexity.

5   For the analysis of gravity waves, we estimated wave energy and wave action from the horizontal divergence. This approach does not require an explicit numerical filtering which is a practical advantage. Other methods for the analysis of unbalanced flow components are available, although more complicated (Mirzaei et al., 2017). While the chosen formulae requires the variance (or squared amplitude) and wave numbers, UWaDi may also provide local estimates for more complex tools such as the combined Rossby wave and gravity wave diagnostics of Kinoshita and Sato (2013). There, cross-covariances of different

10   quantities are needed. For our study, which is focused on GWs, the specific approach is optimal.

With the short analysis of the synoptic situation on 30 January 2016 we show the advantages of UWaDi: providing wave quantities on every grid point. Longitude-dependent GW filter processes, known as selective wave transmission, can be analysed in detail. We find that in zonal mean no prominent GW features can be seen during a mSSW vortex displacement. Instead, local vertical profiles show selective wave transmissions relative to the zonal mean profiles. During strong eastward winds GW

15   propagation is high at all altitudes, the vertical wave number does not show strong variation, thus indicating a steadily vertical propagation of GWs. We find the source of the GWs in the troposphere and characterise this case as induced by flow over orography. Further, critical layer absorption is visible. The wave case with overall low zonal wind reveals gradients in wave action at the altitude of a wind reversal. Unexpectingly, we see the influence of the ECMWF sponge layer in the stratosphere which starts to flatten GWs at an altitude of 35 km in situations of weak winds and slow waves. In an area where the wind field

20   is effected by the mSSW, we find a curved and decelerating jet stream-exit region in the stratosphere and suggest that GWs are emitted there. With the present method we plan to join the closer evaluation of observations and models with respect to local features of GW generation and propagation.

Appendix A: Estimates for two-wave mixture

In this section we illustrate mathematically the amplitude and wave number estimate for a superposition of waves. For simplicity, imagine a mixture of two waves

$$f = a_1 \cos(k_1 x + \phi_1) + a_2 \cos(k_2 x + \phi_2). \tag{A1}$$

The Hilbert transform creates

$$H = a_1 \sin(k_1 x + \phi_1) + a_2 \sin(k_2 x + \phi_2). \tag{A2}$$

The amplitude is calculated by

$$a^2 = f^2 + H^2 \tag{A3}$$

5   and contains mixed-wavelengths which are either slow $(\pm(k_1 - k_2))$ or fast $(\pm(k_1 + k_2))$. The application of the low-pass filter (Step 8) is intented to eliminate the fast spurious components which are expected to create the most fuzziness. With this procedure supposed to work we find from the equal-wave number termn the sum of all squared amplitudes

$$a^2 = a_1^2 + a_2^2. \tag{A4}$$

This means: all variance is included in this estimate. For the wave numbers we find from the definition

10    $$k^2 = \frac{k_1^2 a_1^2 + k_2^2 a_2^2}{a_1^2 + a_2^2}. \tag{A5}$$

This is the amplitude-weighted sum of squared wave numbers.

The covariance (or squared standard deviation) is the mean of squares:

$$s^2 = \langle f^2 \rangle = \langle a_1^2 \cos^2(k_1 x + \phi_1) + a_2^2 \cos^2(k_2 x + \phi_2) \rangle = \frac{a_1^2}{2} + \frac{a_2^2}{2} = \frac{a^2}{2} \tag{A6}$$

15   Hence, the ensemble average results in half of the squared amplitude.

Appendix B: Derivation of kinematic wave energy

The total energy is composed of kinetic and potential energy $(e_{tot} = e_{kin} + e_{pot})$. We use the polarisation equations for hydrostatic GWs to express the kinetic energy with horizontal divergence $\delta = -\mathrm{i}(k_x u + k_y v)$ and vorticity $\xi = -\mathrm{i}(k_x u - k_y v)$ as

20    $$e_{kin} = \frac{1}{2}(u^2 + v^2) = \frac{1}{2} \frac{\delta^2 + \xi^2}{k_h^2}. \tag{B1}$$

The potential energy is expressed with the buoyancy tendency $-\mathrm{i}\omega b = -N^2 w$ to yield

$$e_{pot} = \frac{1}{2} \frac{b^2}{N^2} = \frac{1}{2} \frac{N^2 w^2}{\omega^2} \tag{B2}$$

in order to express the total energy in terms of the divergence, both formulae are combined with the vorticity tendency $-\mathrm{i}\xi = -f\delta$ and the continuity equation $(\delta = \mathrm{i}k_z w)$ for

25    $$e_{tot} = \frac{1}{2}\left(\frac{\delta^2}{k_h^2}\left(1 + \frac{f^2}{\omega^2}\right) + \frac{N^2}{\omega^2}\frac{\delta^2}{k_z^2} \right). \tag{B3}$$

The final result is obtained with incorporation of the disperion relation $\omega^2 = f^2 + N^2 \frac{k_h^2}{k_z^2}$ reading

$$e_{tot} = \frac{\delta^2}{k_h^2}. \tag{B4}$$

References

Albers, J. R. and Birner, T.: Vortex preconditioning due to planetary and gravity waves prior to sudden stratospheric warmings, Journal of the Atmospheric Sciences, 71, 4028–4054, 2014.

Alexander, M. J. and Vincent, R. A.: Gravity waves in the tropical lower stratosphere: A model study of seasonal and interannual variability, Journal of Geophysical Research: Atmospheres, 105, 17 983–17 993, 2000.

Andrews, D. G., Holton, J. R., and Leovy, C. B.: Middle atmosphere dynamics, 40, Academic press, 1987.

Bretherton, F. P.: The propagation of groups of internal gravity waves in a shear flow, Quarterly Journal of the Royal Meteorological Society, 92, 466–480, 1966.

Butler, A. H., Seidel, D. J., Hardiman, S. C., Butchart, N., Birner, T., and Match, A.: Defining sudden stratospheric warmings, Bulletin of the American Meteorological Society, 96, 1913–1928, 2015.

Chatfield, C.: The analysis of time series: an introduction, CRC press, 2016.

Coy, L., Newman, P. A., Pawson, S., and Lait, L. R.: Dynamics of the Disrupted 2015/16 Quasi-Biennial Oscillation, Journal of Climate, 30, 5661–5674, 2017.

Dörnbrack, A., Pitts, M. C., Poole, L. R., Orsolini, Y. J., Nishii, K., and Nakamura, H.: The 2009-2010 arctic stratospheric winter-general evolution, mountain waves and predictability of an operational weather forecast model, Atmospheric Chemistry and Physics, 12, 3659, 2012.

Dörnbrack, A., Gisinger, S., Pitts, M. C., Poole, L. R., and Maturilli, M.: Multilevel cloud structures over Svalbard, Monthly Weather Review, 145, 1149–1159, 2017.

Dunkerton, T. J.: The role of gravity waves in the quasi-biennial oscillation, Journal of Geophysical Research: Atmospheres, 102, 26 053–26 076, 1997.

Dunkerton, T. J. and Butchart, N.: Propagation and selective transmission of internal gravity waves in a sudden warming, Journal of the Atmospheric Sciences, 41, 1443–1460, 1984.

ECMWF: Part III: Dynamics and Numerical Procedures, IFS Documentation, ECMWF, 2016.

Ehard, B., Kaifler, B., Dörnbrack, A., Preusse, P., Eckermann, S. D., Bramberger, M., Gisinger, S., Kaifler, N., Liley, B., Wagner, J., et al.: Horizontal propagation of large-amplitude mountain waves into the polar night jet, Journal of Geophysical Research: Atmospheres, 122, 1423–1436, 2017.

Ern, M. and Preusse, P.: Gravity wave momentum flux spectra observed from satellite in the summertime subtropics: Implications for global modeling, Geophysical Research Letters, 39, doi:10.1029/2012GL052659, 115810, 2012.

Ern, M., Ploeger, F., Preusse, P., Gille, J., Gray, L., Kalisch, S., Mlynczak, M., Russell, J., and Riese, M.: Interaction of gravity waves with the QBO: A satellite perspective, Journal of Geophysical Research: Atmospheres, 119, 2329–2355, 2014.

Ern, M., Thai, Q., John, C., Martin, G., James, M., and Michael, J.: Satellite observations of middle atmosphere gravity wave absolute momentum flux and of its vertical gradient during recent stratospheric warmings, Atmos. Chem. Phys, 1680, 7324, 2016.

Ern, M., Hoffmann, L., and Preusse, P.: Directional gravity wave momentum fluxes in the stratosphere derived from high-resolution AIRS temperature data, Geophysical Research Letters, 44, 475–485, 2017.

Fritts, D. C. and Alexander, M. J.: Gravity wave dynamics and effects in the middle atmosphere, Reviews of Geophysics, 41, doi:10.1029/2001RG000106, 1003, 2003.

Garcia, R. R. and Solomon, S.: The effect of breaking gravity waves on the dynamics and chemical composition of the mesosphere and lower thermosphere, Journal of Geophysical Research: Atmospheres, 90, 3850–3868, 1985.

Glatt, I. and Wirth, V.: Identifying Rossby wave trains and quantifying their properties, Quarterly Journal of the Royal Meteorological Society, 140, 384–396, 2014.

5 Guest, F. M., Reeder, M. J., Marks, C. J., and Karoly, D. J.: Inertia–gravity waves observed in the lower stratosphere over Macquarie Island, Journal of the Atmospheric Sciences, 57, 737–752, 2000.

Holton, J. R.: The Influence of Gravity Wave Breaking on the General Circulation of the Middle Atmosphere, Journal of the Atmospheric Sciences, 40, 2497–2507, 1983.

Jablonowski, C. and Williamson, D. L.: The pros and cons of diffusion, filters and fixers in atmospheric general circulation models, in: 10 Numerical Techniques for Global Atmospheric Models, pp. 381–493, Springer, 2011.

Jewtoukoff, V., Hertzog, A., Plougonven, R., de la Cámara, A., and Lott, F.: Comparison of gravity waves in the Southern Hemisphere derived from balloon observations and the ECMWF analyses, Journal of the Atmospheric Sciences, 2015.

Kalisch, S., Preusse, P., Ern, M., Eckermann, S. D., and Riese, M.: Differences in gravity wave drag between realistic oblique and assumed vertical propagation, Journal of Geophysical Research: Atmospheres, 119, 10,081–10,099, doi:10.1002/2014JD021779, 2014.

15 Khaykin, S., Hauchecorne, A., Mzé, N., and Keckhut, P.: Seasonal variation of gravity wave activity at midlatitudes from 7 years of COSMIC GPS and Rayleigh lidar temperature observations, Geophysical Research Letters, 42, 1251–1258, 2015.

Kinoshita, T. and Sato, K.: A formulation of three-dimensional residual mean flow applicable both to inertia–gravity waves and to Rossby waves, Journal of the Atmospheric Sciences, 70, 1577–1602, 2013.

Kramer, R., Wüst, S., Schmidt, C., and Bittner, M.: Gravity wave characteristics in the middle atmosphere during the CESAR campaign at 20 Palma de Mallorca in 2011/2012: Impact of extratropical cyclones and cold fronts, Journal of Atmospheric and Solar-Terrestrial Physics, 128, 8–23, 2015.

Krisch, I., Preusse, P., Ungermann, J., Dörnbrack, A., Eckermann, S. D., Ern, M., Friedl-Vallon, F., Kaufmann, M., Oelhaf, H., Rapp, M., Strube, C., and Riese, M.: First tomographic observations of gravity waves by the infrared limb imager GLORIA, Atmospheric Chemistry and Physics Discussions, 2017, 1–21, 2017.

25 Lehmann, C., Kim, Y.-H., Preusse, P., Chun, H.-Y., Ern, M., and Kim, S.-Y.: Consistency between Fourier transform and small-volume few-wave decomposition for spectral and spatial variability of gravity waves above a typhoon, Atmospheric Measurement Techniques, 5, 1637–1651, 2012.

Limpasuvan, V., Alexander, M. J., Orsolini, Y. J., Wu, D. L., Xue, M., Richter, J. H., and Yamashita, C.: Mesoscale simulations of gravity waves during the 2008–2009 major stratospheric sudden warming, Journal of Geophysical Research: Atmospheres, 116, 2011.

30 Liu, H.-L. and Roble, R. G.: A study of a self-generated stratospheric sudden warming and its mesospheric–lower thermospheric impacts using the coupled TIME-GCM/CCM3, Journal of Geophysical Research: Atmospheres, 107, ACL 15–1–ACL 15–18, doi:10.1029/2001JD001533, 4695, 2002.

Manney, G. L. and Lawrence, Z. D.: The major stratospheric final warming in 2016: dispersal of vortex air and termination of Arctic chemical ozone loss, Atmospheric Chemistry and Physics, 16, 15 371, 2016.

35 Matthias, V., Dörnbrack, A., and Stober, G.: The extraordinarily strong and cold polar vortex in the early northern winter 2015/2016, Geophysical Research Letters, 43, 2016.

Mirzaei, M., Zülicke, C., Mohebalhojeh, A. R., Ahmadi-Givi, F., and Plougonven, R.: Structure, energy, and parameterization of inertia–gravity waves in dry and moist simulations of a baroclinic wave life cycle, Journal of the Atmospheric Sciences, 71, 2390–2414, 2014.

Mirzaei, M., Mohebalhojeh, A. R., Zülicke, C., and Plougonven, R.: On the quantification of imbalance and inertia-gravity waves generated in numerical simulations of moist baroclinic waves using the WRF model, Journal of the Atmospheric Sciences, in press, doi:10.1175/JAS-D-16-0366.1, 2017.

Plougonven, R., Teitelbaum, H., and Zeitlin, V.: Inertia gravity wave generation by the tropospheric midlatitude jet as given by the Fronts and Atlantic Storm-Track Experiment radio soundings, Journal of Geophysical Research: Atmospheres, 108, doi:10.1029/2003JD003535, 4686, 2003.

Preusse, P., Ern, M., Bechtold, P., Eckermann, S., Kalisch, S., Trinh, Q., and Riese, M.: Characteristics of gravity waves resolved by ECMWF, Atmospheric Chemistry and Physics, 14, 10 483–10 508, 2014.

Schönwiese, C.-D.: Praktische Statistik für Meteorologen und Geowissenschaftler, Schweizerbart'sche Verlagsbuchhandlung, 2013.

Shutts, G. and Vosper, S.: Stratospheric gravity waves revealed in NWP model forecasts, Quarterly Journal of the Royal Meteorological Society, 137, 303–317, 2011.

Smith, S. W. et al.: The scientist and engineer's guide to digital signal processing, 1997.

Stober, G., Matthias, V., Jacobi, C., Wilhelm, S., Höffner, J., and Chau, J. L.: Exceptionally strong summer-like zonal wind reversal in the upper mesosphere during winter 2015/16, Annales Geophysicae, 35, 711–720, 2017.

Thurairajah, B., Collins, R. L., Harvey, V. L., Lieberman, R. S., Gerding, M., Mizutani, K., and Livingston, J. M.: Gravity wave activity in the Arctic stratosphere and mesosphere during the 2007–2008 and 2008–2009 stratospheric sudden warming events, Journal of Geophysical Research: Atmospheres, 115, 2010.

Uccellini, L. and Koch, S.: The synoptic setting and possible source mechanisms for mesoscale gravity wave events, Mon. Weather Rev, 115, 721–729, 1987.

Vincent, R. A. and Fritts, D. C.: A climatology of gravity wave motions in the mesopause region at Adelaide, Australia, Journal of the Atmospheric Sciences, 44, 748–760, 1987.

Von Storch, H. and Zwiers, F. W.: Statistical analysis in climate research, Cambridge university press, 2001.

Wang, L. and Alexander, M. J.: Gravity wave activity during stratospheric sudden warmings in the 2007–2008 Northern Hemisphere winter, Journal of Geophysical Research: Atmospheres, 114, doi:10.1029/2009JD011867, d18108, 2009.

Wright, C. J., Hindley, N. P., Hoffmann, L., Alexander, M. J., and Mitchell, N. J.: Exploring gravity wave characteristics in 3-D using a novel S-transform technique: AIRS/Aqua measurements over the Southern Andes and Drake Passage, Atmospheric Chemistry and Physics, 17, 8553, 2017.

Yamashita, C., Liu, H.-L., and Chu, X.: Gravity wave variations during the 2009 stratospheric sudden warming as revealed by ECMWF-T799 and observations, Geophysical Research Letters, 37, doi:10.1029/2010GL045437, l22806, 2010.

Yamashita, C., England, S. L., Immel, T. J., and Chang, L. C.: Gravity wave variations during elevated stratopause events using SABER observations, Journal of Geophysical Research: Atmospheres, 118, 5287–5303, 2013.

Zimin, A. V., Szunyogh, I., Patil, D., Hunt, B. R., and Ott, E.: Extracting envelopes of Rossby wave packets, Monthly Weather Review, 131, 1011–1017, 2003.

Zimin, A. V., Szunyogh, I., Hunt, B. R., and Ott, E.: Extracting envelopes of nonzonally propagating Rossby wave packets, Monthly Weather Review, 134, 1329–1333, 2006.

Zülicke, C. and Peters, D.: Simulation of inertia-gravity waves in a poleward-breaking Rossby wave, Journal of the Atmospheric Sciences, 63, 3253–3276, 2006.